ESIPT-Active cinnamoyl pyrones are bright solid-state emitters: Revisited theoretical approach and experimental study

Emma Bremond, Martial Boggio-Pasqua, Nadine Leygue, Mokhtar Fodili, Pascal Hoffmann, Nathalie Merceron-Saffon, Rémi Métivier, Suzanne Fery-Forgues

ESIPT-Active cinnamoyl pyrones are bright solid-state emitters: Revisited theoretical approach and experimental study

Emma Bremond [a], Martial Boggio-Pasqua [b], Nadine Leygue [a], Mokhtar Fodili [c], Pascal Hoffmann [a], Nathalie Saffon-Merceron [d], Rémi Métivier [e], Suzanne Fery-Forgues [a]*

[a] *Laboratoire SPCMIB, CNRS UMR 5068, Université de Toulouse III Paul Sabatier, 118 route de Narbonne, 31062 Toulouse cedex 9, France*

[b] *Laboratoire de Chimie et Physique Quantiques (LCPQ), CNRS UMR 5626, Université de Toulouse III Paul Sabatier, 118 route de Narbonne, 31062 Toulouse cedex 9, France*

[c] *Laboratoire de Recherche de Chimie Organique et Substances Naturelles, Université de Djelfa, Algeria*

[d] *Service commun RX, Institut de Chimie de Toulouse, ICT- UAR2599, Université de Toulouse III Paul Sabatier, 31062 Toulouse cedex 9, France*

[e] *Université Paris-Saclay, ENS Paris-Saclay, CNRS, Photophysique et Photochimie Supramoléculaires et Macromoléculaires, 91190 Gif-sur-Yvette, France*

*Corresponding author. E-mail: suzanne.fery-forgues@univ-tlse3.fr

Electronic supplementary information (ESI) available: Chemical characterization data, crystallographic data, computational data, photoluminescence spectra and decays.

Keywords: Aggregation induced emission (AIE); solid state luminescence enhancement (SLE); ESIPT; photoluminescence; crystal structure; SF-TD-DFT

Abbreviations:
AIE: Aggregation induced emission
SLE: Solid-state luminescence enhancement
ESIPT: Excited-state intramolecular proton transfer
SF-TD-DFT: Spin-flip time-dependent density functional theory
ICT: Intramolecular charge transfer
TICT: Twisted intramolecular charge transfer
CI: Conical intersection

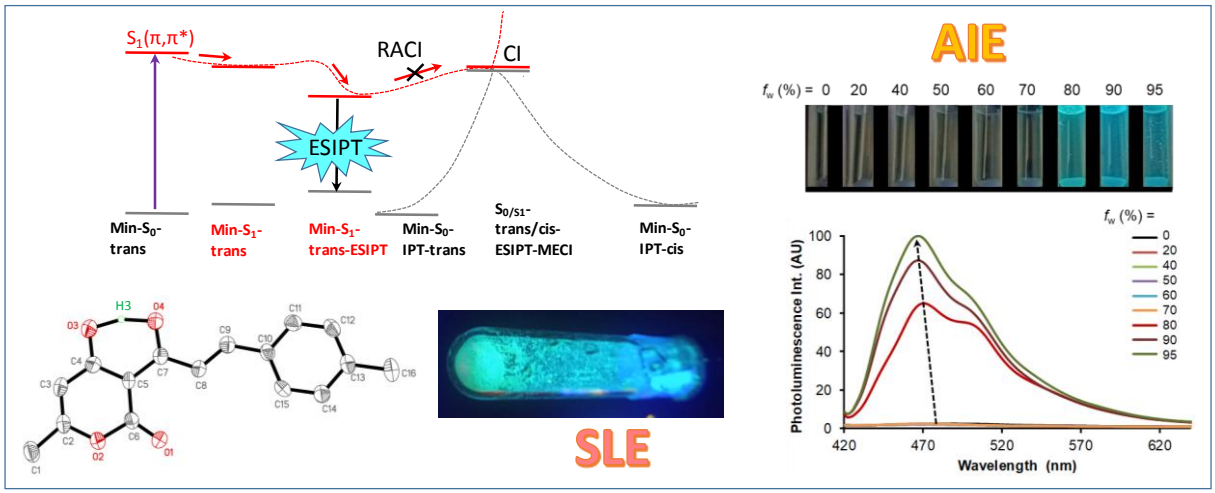

ABSTRACT
Excited-state intramolecular proton transfer (ESIPT) is a photophysical process that may lead to superior emission properties. For a long time, cinnamoyl pyrone (CP) derivatives have been classified as non-ESIPT molecules. With the exception of those bearing a strong electron-donor substituent, they have been considered to have no interest from a spectroscopic point of view, because they are virtually not fluorescent in solution. Revisiting their photophysical behaviour in solution shows the complexity of the mechanisms involved. It appeared that CPs with no or weak electron-donor substituents indeed undergo ESIPT, but the facile access to a conical intersection subsequently induces non-radiative deactivation, hence the extinction of fluorescence in solution. When substituted by an electron-donating diethylamino group, the molecules deactivate through a radiative intramolecular charge transfer (ICT) state following an ESIPT process. In the solid state, the restricted access to conical intersection (RACI) makes most of the CP derivatives strongly fluorescent. Whatever the electron-donating strength of their substituent, most of these molecules become good emitters in the solid state, with emission ranging from turquoise blue to deep red. Although they need extensive purification, their one-step synthesis and spectacular aggregation-induced emission (AIE) properties make these molecules good candidates for applications in the field of AIE-probes and photoluminescent materials.

1. Introduction

Molecules that exhibit solid-state luminescence enhancement (SLE), *i.e.* the property to be more strongly emissive in the various solid states than in solution, find an increasing number of applications in the fields of optoelectronic and nanophotonic devices, high-performance functionalized luminescent materials, biological imaging and theranostics [1]. Those emitting in the red are of particular interest for full-colour displays and super-resolution imaging [2, 3]. Dramatic advances have been made in this field from 2001 with the development of special molecular frameworks that promote efficient aggregation-induced emission (AIE) [4–6]. Prototypical AIE-fluorogens are large rotor molecules such as tetraphenylethene and pentaphenylsilole, which emit in the blue and green wavelength range [7]. However, subsequent chemical modifications are necessary to shift the emission towards long wavelengths. The demanding and complex synthesis is then a major drawback of this approach. It is therefore of great interest to look for SLE-active organic molecules that can be obtained in high yields from facile and economic synthesis.

Regarding small solid-state emitters, one of the smartest red-shifting strategies is based on the combination of intramolecular charge transfer (ICT), commonly found in donor-π-acceptor molecules, and excited-state intramolecular proton transfer (ESIPT), a photochemical process leading to the formation of a keto tautomer that emits fluorescence at much longer wavelengths than the initial enol form [8–12]. It has been reported that many molecules with ESIPT properties are strongly fluorescent in the solid state, and even show SLE properties, enhanced by the molecular planarization and stiffening due to ESIPT. However, designing this type of molecule for use in the solid state remains a challenge. In fact, the ESIPT process competes with other photophysical processes, and the balance of powers may be very different in solution and in the solid state. Besides, the photoluminescence (PL) properties, which closely depend on the intermolecular interactions and packing mode, are very sensitive to the smallest structural variation and therefore difficult to predict.

2-(2'-Hydroxyphenyl)benzazole derivatives are the typical example of molecules whose SLE properties result from both ICT and ESIPT [13]. By comparison, 2'-hydroxychalcones are much less popular. However, the derivatives bearing a dialkylamino group in the *para* position of the phenyl ring, such as **HC1,** which has been reported for a long time to exhibit ESIPT fluorescence in solution [14, 15], and some of its analogues (*e.g.* **HC2** and **HC3**), have recently proven to be valuable SLE probes that emit intense orange-red ESIPT luminescence, particularly sensitive to the crystal packing mode [16, 17]. 2'-Hydroxychalcone derivatives are potentially usable for the detection of alkaline phosphatase activity [18] and for the development of organic lasers [17].

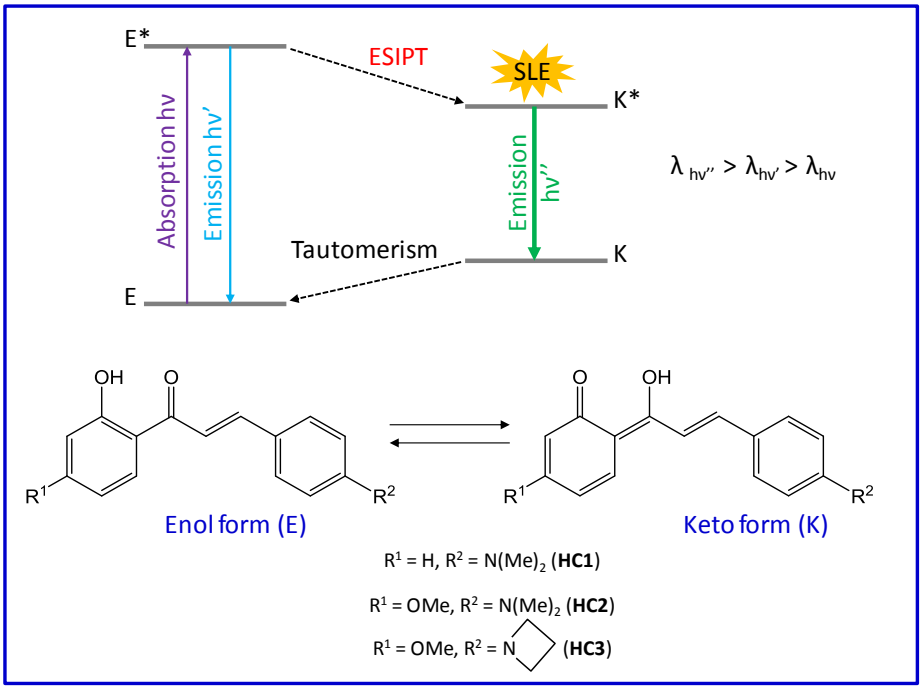

Scheme 1. Chemical structure of SLE-active 2'-hydroxychalcone derivatives [16, 17] in the enol (E) and keto (K) forms, and photophysical process featuring ESIPT.

Curiously, these properties have not been sought after in the closely-related family of cinnamoyl pyrones (CP), the first member of which is compound **1** (Scheme 2). CP derivatives have biological [19] and antimicrobial activity [20]. They have been used as intermediates in the synthesis of pharmacologically-active pyrazole-based molecules [21], benzodiazepines [22] and antitubercular agents [23], as well as in the preparation of fluorescent probes for the detection of amyloid fibrils [24]. From a spectroscopic point of view, CP derivatives have only been studied in solution. Roshal and coworkers divided them into two groups depending on the nature of the substituent in the *para*-position of the phenyl ring [25–27]. Those with strong electron-donating dialkylamino group would be well fluorescent in weakly polar organic solvents owing to a lowest lying ππ* excited state. In fact, Benosmane *et al*. have observed that the position of the emission spectra of these compounds correlates well with a solvent polarity scale, while the intensity strongly decreases in the most polar solvents [28], which suggests the involvement of conventional ICT. In contrast, CPs bearing neutral or weak electron-donating substituents have been classified as virtually not emissive, which would be due to the nπ* character of the low-energy excited state. This state would lead to efficient intersystem crossing that turns off the fluorescence emission in solution, and induces weak phosphorescence emission in polymer matrixes. On the bases of

both experimental and theoretical work, it seems that ESIPT cannot be expected from any of these molecules [25–27], although the hydroxyl and carbonyl group are properly displayed to form a six-membered ring after proton transfer. Consequently, due to their poor spectroscopic performance, CPs have attracted very little attention until now, and to the best of our knowledge, their solid-state properties have not been studied.

However, the structural similarity between 2'-hydroxychalcone and CPs suggests that the latter compounds deserve being studied in the solid state. Seven CP derivatives (**1**−**7**), differing by the substituent in the *para* position of the phenyl group, were thus prepared, as well as the methoxylated analogues **8** and **9**, used for the sake of comparison (Scheme 2). Crystal structures were obtained and discussed. From a spectroscopic viewpoint, most of the CPs emitted in the microcrystalline state, much more efficiently than their methoxylated analogues. Remarkably, the colour of the light emitted by the CPs covers the entire visible spectrum while only a very small structural modification has been brought to their chemical structure. The photophysical mechanism was revisited owing to quantum chemical calculations, showing the involvement of the ESIPT process among other photophysical mechanisms. It appears that CP derivatives, which can be obtained in the gram scale via a one-pot reaction, are very attractive candidates for use as solid-state luminescent materials.

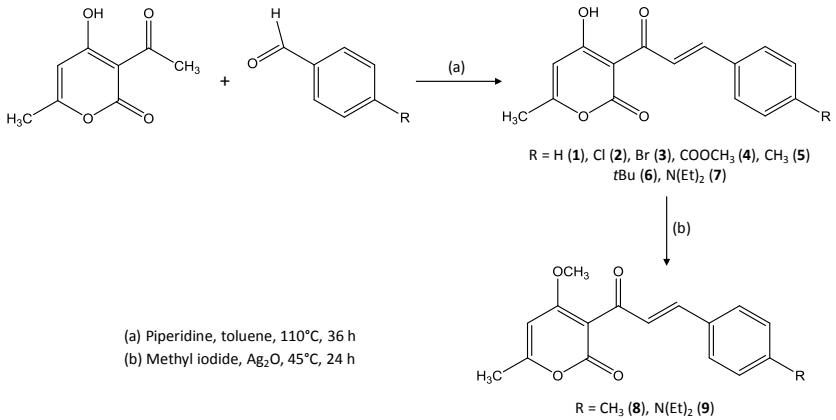

Scheme 2. Synthesis and chemical structure of the cinnamoyl pyrone derivatives **1**−**7** and their methoxylated analogues **8** and **9** studied in this work.

2. Experimental section

2.1. Materials

All reagent grade chemicals obtained from Sigma-Aldrich (4-methylbenzaldehyde and 4-(*tert*-butyl)benzaldehyde) and Alfa Aesar (dehydroacetic acid and methyl-4-formylbenzoate) were used without further purification. Extra dry toluene (99.8 %) from Acros Organics, as well as dichloromethane and petroleum ether from Fisher Scientific and acetonitrile from Honeywell were used as received. The reactions were monitored by thin-layered chromatography (TLC) using 0.2 mm Alugram Xtra silica gel 60 F254 pre-coated sheets. Purifications by flash chromatography were made using a silica column (porosity 30 µm) purchased from Interchim.

2.2. Synthesis of the cinnamoyl pyrones derivatives

Compounds **1**–**3**, obtained from a former work [23], were purified by flash chromatography on silica column using dichloromethane/petroleum ether (8:2) as eluent system for **2** and **3**, and dichloromethane for **1**.

For the synthesis of compounds **4**–**7** (Scheme 2), to a solution of dehydroacetic acid (0.50 g, 2.98 mmol) in dry toluene (6 mL) was added the corresponding aldehyde (3 mmol). Piperidine (0.04 g, 0.47 mmol) was added dropwise. The reaction mixture was heated to reflux under argon for 36 h and then the toluene was removed under reduced pressure. The oily residue obtained was dissolved in dichloromethane and washed with water. The combined organic layers were dried over anhydrous $MgSO_4$ and the solvent was removed under reduced pressure. Oily residues were obtained for the four compounds. Compound **6** was triturated in ethanol to get a precipitate, which was collected by filtration, and then recrystallized in ethanol. All compounds were then purified by flash chromatography on silica column using dichloromethane/petroleum ether (8:2) for **4** and **7**, and (1:1) for **5** and **6** as eluent system. Compounds **4**–**6** were obtained as yellow powders. For compound **7,** the red solid issued from chromatography was subsequently recrystallized three times in ethanol to give a dark pink powder.

3-[(*E*)-3-(4-Methylbenzoate)prop-2-enoyl]-4-hydroxy-6-methyl-pyran-2-one (**4**)
Yield: 57%. Mp = 161°C. FT-IR (cm^{-1}): 3096, 2952, 2849, 1715, 1632, 1539. ^{1}H NMR ($CDCl_3$, 300 MHz): δ ppm = 2.24 (s, 3H, H7), 3.89 (s, 3H, H16), 5.93 (s, 1H, H5), 7.64–7.70 (m, 2H, H13), 7.85 (d, *J* = 15.8 Hz, 1H, H10), 7.98–8.04 (m, 2H, H12), 8.30 (d, *J* = 15.8 Hz, 1H, H9). ^{13}C NMR ($CDCl_3$, 75 MHz): δ ppm = 20.7 (CH_3, C7), 52.3 (CH_3, C16), 99.6 (Cq, C3), 102.2 (CH, C5), 125.3 (CH, C9), 128.9 (CH, C13), 130.0 (CH, C12), 131.8 (Cq, C11), 138.8 (Cq, C14), 144.3 (CH, C10), 161.1 (Cq, C2), 166.4 (Cq, C15), 169.0 (Cq, C6), 182.9 (Cq, C4), 192.6 (Cq, C8). MS/DCI (CH_4), m/z calcd for $[C_{17}H_{14}O_6 + H]^+$ = 315.0869, found 315.0866. Anal. calcd (%) for $C_{17}H_{14}O_6$: C 64.97, H 4.49; found: C 63.54, H 4.62.

3-[(*E*)-3-(4-Methylbenzene)prop-2-enoyl]-4-hydroxy-6-methyl-pyran-2-one (**5**)
Yield: 60%. Mp = 146 °C. FT-IR (cm^{-1}): 3093, 2968, 2921, 2854, 1716, 1644, 1622, 1604, 1520, 1510, 1483. ^{1}H NMR ($CDCl_3$, 300 MHz): δ ppm = 2.27 (s, 3H, H7), 2.39 (s, 3H, H15), 5.94 (s, 1H, H5), 7.20–7.25 (m, 2H, H13), 7.56–7.62 (m, 2H, H12), 7.96 (d, *J* = 15.7 Hz, 1H, H10), 8.27 (d, *J* = 15.7 Hz, 1H, H9). ^{13}C NMR ($CDCl_3$, 75 MHz): δ ppm = 20.6 (CH_3, C7), 21.6 (CH_3, C15), 99.4 (Cq, C3), 102.5 (CH, C5), 121.8 (CH, C9), 129.3 (CH, C12), 129.7 (CH, C13), 132.0 (Cq, C11), 141.9 (Cq, C14), 146.6 (CH, C10), 161.2 (Cq, C2), 168.5 (Cq, C6), 183.2 (Cq, C4), 192.7 (Cq, C8). HRMS (ESI^+): m/z calcd for $[C_{16}H_{14}O_4 + H]^+$ = 271.0970, found 271.0976. Anal. calcd (%) for $C_{16}H_{14}O_4$: C 71.10, H 5.22, N 10.63; found: C 70.34, H 5.29.

3-[(*E*)-3-((4-*tert*-Butyl)benzene)prop-2-enoyl]-4-hydroxy-6-methyl-pyran-2-one (**6**)
Yield: 56%. Mp = 118 °C. FT-IR (cm^{-1}): 3092, 2954, 2907, 2869, 1717, 1643, 1622, 1605, 1517, 1483. ^{1}H NMR ($CDCl_3$, 300 MHz): δ ppm = 1.34 (s, 9H, H16), 2.27 (s, 3H, H7), 5.95 (s, 1H, H5), 7.40–7.46 (m, 2H, H13), 7.60–7.66 (m, 2H, H12), 7.97 (d, *J* = 15.7 Hz, 1H, H10), 8.29 (d, *J* = 15.7 Hz, 1H, H9). ^{13}C NMR ($CDCl_3$, 75 MHz): δ ppm = 20.8 (CH_3, C7), 31.2 (CH_3, C16), 35.1 (Cq, C15), 99.5 (Cq, C3), 102.6 (CH, C5), 122.2 (CH, C9), 126.1 (CH, C13), 129.3 (CH, C12), 132.1 (Cq, C11), 146.6 (CH, C10), 155.1 (Cq, C14), 161.4 (Cq, C2), 168.6 (Cq, C6), 183.4 (Cq, C4), 192.8 (Cq, C8). MS/DCI (CH_4): m/z calcd for $[C_{19}H_{20}O_4$ +

H]$^+$ = 313.1440, found 313.1438. Anal. calcd (%) for $C_{19}H_{20}O_4$: C 73.06, H 6.45; found: C 71.93, H 6.68.

3-[(*E*)-3-((4-Diethylamino)benzene)prop-2-enoyl]-4-hydroxy-6-methyl-pyran-2-one (**7**)
Yield: 57%. Mp = 158 °C. FT-IR (cm^{-1}): 3092, 2977, 1707, 1641, 1586, 1497, 1465. ^{1}H NMR ($CDCl_3$, 300 MHz): δ ppm = 1.21 (t, 6H, H16), 2.25 (s, 3H, H7), 3.43 (q, 4H, H15), 5.90 (s, 1H, H5), 6.63–6.68 (m, 2H, H13), 7.57–7.62 (m, 2H, H12), 8.00 (d, *J* = 15.5 Hz, 1H, H10), 8.10 (d, *J* = 15.3 Hz, 1H, H9). ^{13}C NMR ($CDCl_3$, 75 MHz): δ ppm = 12.6 (CH3, C16), 20.4 (CH_3, C7), 44.6 (CH_2, C15), 98.8 (Cq, C3), 103.2 (CH, C5), 111.2 (CH, C13), 115.5 (CH, C9), 121.9 (Cq, C11), 132.1 (CH, C12), 148.4 (CH, C10), 150.5 (Cq, C14), 161.5 (Cq, C2), 167.1 (Cq, C6), 183.9 (Cq, C4), 190.9 (Cq, C8). HRMS (ESI$^+$): m/z calcd for [$C_{19}H_{21}NO_4$ + H]$^+$ = 328.1549, found 328.1555. Anal. calcd (%) for $C_{19}H_{21}NO_4$: C 69.71, H 6.47, N 4.28; found: C 69.09, H 6.56, N 4.30.

Compounds **8** and **9** were obtained from **5** and **7**, respectively, using a procedure described in the literature [29]. For the synthesis of **8**, a mixture of compound **5** (50 mg, 0.184 mmol), silver oxide (52 mg, 0.225 mmol) and methyl iodide (0.6 mL) was heated at 45°C in a sealed tube for 24 h, and then the methyl iodide was removed under reduced pressure. Compound **8** was purified by chromatography on silica column using dichloromethane/ ether (95:5) as eluent system. Compound **9** was synthesized similarly starting from 185 mg (0.565 mmol) of compound **7**, 143 mg (0.622 mmol) silver oxide and 1 mL methyl iodide. It was purified by chromatography on silica column using ethyl acetate as eluent.

3-[(*E*)-3-(4-Methylbenzene) prop-2-enoyl]-4-hydroxymethyl-6-methyl-pyran-2-one (**8**)
Yield: 38 %. FT-IR (cm^{-1}): 3088, 2958, 2923, 2853, 1701, 1652, 1586, 1466. ^{1}H NMR ($CDCl_3$, 300 MHz): δ ppm = 2.32 (s, 3H, H7), 2.35 (s, 3H, H15), 3.91 (s, 3H, H16), 6.12 (d, *J* = 0.9 Hz, 1H, H5), 7.05 (d, *J* = 15.9 Hz, 1H, H9), 7.20-7.13 (m, 2H, H13), 7.48-7.42 (m, 2H, H12), 7.56 (d, *J* = 16.0 Hz, 1H, H10). ^{13}C NMR ($CDCl_3$, 75 MHz): δ ppm = 20.8 (CH_3, C7), 21.5 (CH_3, C15), 57.2 (CH_3, C16), 95.3 (CH, C5), 104.9 (Cq, C3), 125.9 (CH, C9), 128.5 (CH, C13), 129.5 (CH, C12), 131.9 (Cq, C11), 140.9 (Cq, C14), 143.9 (CH, C10), 162.0 (Cq, C2), 166.2 (Cq, C6), 169.8 (Cq, C4), 189.0 (Cq, C8). HRMS (ESI$^+$): m/z calcd for [$C_{17}H_{16}O_4$ + H]$^+$ = 285.1127, found 285.1132. Anal. calcd (%) for $C_{17}H_{16}O_4$: C 71.82, H 5.67; found: C 69.76, H 5.27

3-[(*E*)-3-((4-Diethylamino) benzene)prop-2-enoyl]-4-hydroxymethyl-6-methyl-pyran-2-one (**9**)
Yield: 36 %. Mp = 158 °C. FT-IR (cm^{-1}): 3078, 2970, 2929, 2852, 1700, 1644, 1584, 1549, 1520. ^{1}H NMR ($CDCl_3$, 300 MHz): δ ppm = 1.18 (t, 6H, H16), 2.32 (s, 3H, H7), 3.39 (q, 4H, H15), 3.89 (s, 3H, H17), 6.09 (s, 1H, H5), 6.59-6.62 (m, 2H, H13), 6.84 (d, *J* = 15.5 Hz, 2H, H9), 6.59-6.62 (m, 2H, H12), 7.51 (d, *J* = 15.3 Hz, 1H, H10). ^{13}C NMR ($CDCl_3$, 75 MHz): δ ppm = 12.6 (CH_3, C16), 20.4 (CH_3, C7), 44.5 (CH_2, C15), 57.1 (CH_3, C17), 95.4 (CH, C5), 105.5 (Cq, C3), 111.2 (CH, C13), 121.6 (CH, C9), 130.9 (CH, C12), 137.3 (Cq, C11), 145.9 (CH, C10), 149.7 (Cq, C14), 162.2 (Cq, C2), 165.3 (Cq, C6), 168.8 (Cq, C4), 189.3 (Cq, C4). MS/DCI (CH_4): m/z calcd for [$C_{20}H_{23}NO_4$ + H]$^+$ = 342.1705, found 342.1709. Anal. calcd (%) for $C_{20}H_{23}NO_4$: C 70.36, H 6.79, N 4.10; found: C 68.81, H 6.81, N 4.04.

2.3. Apparatus and methods

The melting points were measured on a Melting Point System MP50 Mettler Toledo apparatus. Chemical characterizations were performed in the relevant services of Institut de Chimie de Toulouse (ICT). The ^{1}H NMR and ^{13}C NMR spectra were recorded on a Bruker AC300 spectrometer operating at 300 MHz and 75 MHz, respectively. Chemical shifts are reported in ppm, with residual protonated solvents as internal references. The NMR spectra together with the schemes for the numbering of protons and carbon atoms for compounds **4**–**9** are given in the ESI (Fig. S1 to S9). High-resolution mass spectra (HRMS) were obtained on a Xevo G2 QTof Waters spectrometer. Infrared spectra were obtained using a Nexus ThermoNicolet FTIR spectrophotometer equipped with a diamond ATR.

Spectroscopic measurements were made using a Xenius SAFAS spectrofluorimeter. All fluorescence spectra were corrected. The quantum yields in solution were measured at 20°C in cells of 1 cm optical pathway, using the classical formula:

$$\Phi_x = (A_s \times F_x \times n_x^2 \times \Phi_s)/(A_x \times F_s \times n_s^2) \quad (1)$$

where A is the absorbance at the excitation wavelength, I the integrated fluorescence intensity and n the refractive index. Subscripts s and x refer to the standard and to the sample of unknown quantum yield, respectively. Coumarin 153 (Φ_s = 0.53) in ethanol was used as the standard [30]. The absorbance of the solutions was equal or below 0.06 at the excitation wavelength. The error on the quantum yield values is estimated to be about 10 %.

The photoluminescence of solid samples was analyzed using a $BaSO_4$ integrating sphere, correction was made using a home-made curve. Solid samples were deposited on a metal holder. The excitation source was scanned in order to evaluate the reflected light for the empty sphere (L_a), the samples facing the source light (L_c) and the sample out of the irradiation beam (L_b). The luminescence spectra were recorded with the sample facing the source light (E_c) and out from direct irradiation (E_b). The PM voltage was adapted to the measurement of reflected light and emission spectra, respectively, and proper correction was applied to take into account the voltage difference. The absolute photoluminescence quantum yield values (Φ_{PL}) were calculated by a method based on the one developed by de Mello et al. [31] using the formula:

$$\Phi_{PL} = [E_c\text{-}(1\text{-}\alpha)E_b]/L_a\alpha \quad (2)$$

with $\alpha = 1\text{-}L_c/L_b$. The error on the Φ_{PL} value was estimated to be about 20%.

Emission decay curves were obtained by the time-correlated single-photon counting (TCSPC) method. The setup was composed of a titanium sapphire Ti:Sa oscillator (Spectra Physics, Maï Taï) emitting pulses of 100 fs duration at 760 nm (80 MHz frequency). The repetition rate was reduced down to 4 MHz by a pulse picker, and non-linear SHG crystals generate the desired wavelength at 380 nm (GWU Lasertechnik, UHG-23-PSK). The beam was then directed to the sample solution after adjusting the excitation power with an intensity attenuator filter wheel. Emitted photons were detected at 90° through a polarizer at the magic angle and a monochromator, by means of a micro-channels plate photomultiplier (MCP-PMT R3809U-50, Hamamatsu), connected to a TCSPC module (SPC-630, Becker & Hickl). Emission decays were finally processed with the help of the global non-linear least-squares minimization method including reconvolution analysis (Globals, Laboratory for Fluorescence Dynamics at the University of California, Irvine).

The microcrystalline samples were observed using a Zeiss Axioskop fluorescence microscope (λ_{ex} = 450−490 nm, λ_{em}> 500 nm) equipped with an Andor Luca camera.

2.4. Crystallography

Crystal data were collected at 193(2) K on a Bruker-AXS APEX II diffractometer equipped with a 30 W air-cooled microfocus source (ImS) with focusing multiplayer optics (compound **5**) and on a Bruker-AXS D8-Venture diffractometer equipped with a Photon III-C14 detector (compounds **1**, **2**, **3** **6**, **7**, **8** and **9**), using MoKα radiation (λ = 0.71073 Å). The structures were solved using an intrinsic phasing method (ShelXT) [32]. All non-hydrogen atoms were refined anisotropically using the least-squares method on F^2 [33]. Molecular graphics were generated using the MERCURY software [34]. Hydrogen atoms were refined isotropically at calculated positions using a riding model with their isotropic displacement parameters constrained to be equal to 1.5 times the equivalent isotropic displacement parameters of their pivot atoms for terminal sp^3 carbon and 1.2 times for all others carbon atoms. H atoms on O were located by difference Fourier maps and freely refined. Selected crystallographic data are collected in Table 1. CCDC-2183755 (**1**), CCDC-2183756 (**2**), CCDC-2183757 (**3**), CCDC-2183758 (**5**), CCDC-2183759 (**6**), CCDC-2183760 (**7**), CCDC-2183761 (**8**) and CCDC-2183762 (**9**) contain the supplementary crystallographic data for these compounds. These data can be obtained free of charge from The Cambridge Crystallographic Data Centre via https://www.ccdc.cam.ac.uk/structures/.

2.5. Theoretical calculations

The ground- and first excited-state potential energy surfaces of the isolated compound **1** were explored using complementary density functional theory (DFT)-based approaches. Time-dependent DFT (TD-DFT) and its spin-flip variant (SF-TD-DFT) were used to investigate the excited-state potential energy surfaces of this representative system. TD-DFT and SF-TD-DFT calculations were performed with the MN15 [35] and BH&HLYP [36] functionals, respectively, and the 6-311+G** basis set. The excited-state transition state was optimized at the TD-DFT level only, for which analytical second derivatives of the energy with respect to nuclear coordinates could be computed. The SF-TD-DFT calculations used a reference triplet state obtained from a restricted open-shell DFT calculation. Conical intersections were optimized only at SF-TD-DFT level, as it allows a correct description of the potential energy surface topology where the ground- and first excited state couple [37]. Effects of the solvent were included within the integral equation formalism polarizable continuum model (IEFPCM) [38]. The external iteration state-specific non-equilibrium approach [39] was used to compute vertical emission energies. Calculations were also performed on compound **2** containing a weak electron-withdrawing substituent and on a model system of compound **7** by replacing the electron-donating diethylamino group by a dimethylamino group. The charge transfer character of the lowest excited state was evaluated by computing the D_{CT} index [40], which gives a measure of the length of the electron transfer associated to an electronic transition. DFT and TD-DFT calculations were performed with Gaussian 16 [41]. Gamess [42] was used for SF-TD-DFT calculations. The geometries (Cartesian coordinates) of optimized structures obtained at TD-DFT and SF-TD-DFT levels are given in Tables S1 to S4.

	1	**2**	**3**	**5**	**6**	**7**	**8**	**9**
Empirical formula	$C_{15}H_{12}O_4$	$C_{15}H_{11}ClO_4$	$C_{15}H_{11}BrO_4$	$C_{16}H_{14}O_4$	$C_{19}H_{20}O_4$	$C_{19}H_{21}NO_4$	$C_{17}H_{16}O_4$	$C_{20}H_{23}NO_4$
Formula weight	256.25	290.69	335.15	270.27	312.35	327.37	284.30	341.39
Crystal system	Monoclinic	Triclinic	Monoclinic	Triclinic	Monoclinic	Monoclinic	Monoclinic	Monoclinic
Space group	$P2_1/c$	$P\bar{1}$	$P2_1$	$P\bar{1}$	Cc	$P2_1/c$	$P2_1/c$	$P2_1/c$
Unit cell dimensions								
a (Å)	11.9829(8)	5.1462(3)	3.9144(3)	7.2990(15)	17.3394(10)	16.0760(13)	7.6260(4)	7.7635(2)
b (Å)	15.1973(9)	9.6514(7)	39.571(3)	13.636(3)	10.5346(7)	17.0969(9)	26.7355(15)	7.4928(3)
c (Å)	20.6256(12)	13.1348(10)	17.1033(12)	15.155(3)	11.0119(13)	13.3865(8)	7.7699(5)	30.5667(12)
α (°)	90	86.694(3)	90	105.819(5)	90	90	90	90
β (°)	102.698(2)	89.630(3)	90.860(2)	102.990(5)	125.4673(13)	114.513(2)	115.0090(19)	94.7660(10)
γ (°)	90	85.656(3)	90	104.283(6)	90	90	90	90
Volume ($Å^3$)	3664.2(4)	649.42(8)	2649.0(3)	1335.6(4)	1638.2(2)	3347.7(4)	1435.64(15)	1771.93(11)
Z	12	2	8	4	4	8	4	4
Crystal size (mm^3)	0.300 × 0.250 × 0.200	0.500 × 0.040 × 0.040	0.400 × 0.050 × 0.040	0.450 × 0.120 × 0.080	0.280 × 0.180 × 0.150	0.300 × 0.200 × 0.150	0.600 × 0.250 × 0.080	0.080 × 0.080 × 0.040
Density (g cm^{-3})	1.393	1.487	1.681	1.344	1.266	1.299	1.315	1.280
Reflections collected/independent	122262/8734	16895/3216	47456/12981	40080/5432	24044/3901	171737/8309	45366/3551	31656 / 5185
R(int)	0.0644	0.0439	0.0520	0.0994	0.0399	0.0967	0.0281	0.0674
Parameters/Restraints	526/0	186/0	732/2	371/0	216/2	448/0	193/0	230/0
Final R_1 indices I > 2σ(I)	0.0656	0.0406	0.0626	0.0589	0.0364	0.0446	0.0522	0.0495
wR_2 all data	0.1713	0.1108	0.1453	0.1948	0.0894	0.1156	0.1373	0.1276
Largest diff. peak and hole (e.$Å^{-3}$)	0.393 and -0.257	0.384 and -0.233	1.356 and -1.879	0.261 and -0.281	0.163 and -0.163	0.293 and -0.196	0.407 and -0.251	0.322 and -0.200
CCDC	2183755	2183756	2183757	2183758	2183759	2183760	2183761	2183762

Table 1. Crystallographic data of cinnamoyl pyrone derivatives

3. Results and discussion

3.1. Synthesis

All compounds were prepared by condensation of dehydroacetic acid and appropriate aldehyde in refluxing dry toluene according to a one pot procedure [43]. Monitoring the reaction progress by TLC and NMR showed that impurities were formed and reagents were not completely consumed after 36 h under the experimental conditions used. Compounds **8** and **9** were obtained by heating the hydroxylated parent compound (**5** and **7**, respectively) at 45°C in a mixture of MeI and Ag_2O for 24 h [28]. All compounds were extensively purified by chromatography, and subsequent recrystallization, otherwise the presence of colored impurities led to major variations of the spectroscopic properties. As a result, yields were around 60% for **4**, **5**, **6** and **7**, and slightly lower than 40% for **8** and **9**.

3.2. Crystallographic study

For most of compounds, good quality single crystals were obtained by slow evaporation of dichloromethane solutions. Only **4** gave tiny needles whatever the crystallization conditions implemented so far, and so the X-ray analysis could not be performed.

The molecular views are given in Fig. S10. All molecules examined are found in *trans* configuration. As all H atoms of hydroxyl groups were located by difference Fourier maps and freely refined, it is possible to compare their position. Noticeably, for CP derivatives **1**–**3** and **5**–**7**, a strong intramolecular hydrogen bond takes place between the carbonyl oxygen atom O(4) and the hydrogen atom H(3) of the hydroxyl group. The length of this H-bond is below 1.7 Å. For the methyl (**5)** and diethylamino (**7**) derivatives (Fig. 1), the hydrogen atom H(3) of the hydroxyl group is situated at almost equal distance (~1.2 Å) from both oxygen atoms O(3) and O(4), thus giving some symmetry to the six-membered ring. The conjugated electron system is relatively planar. Its twisting degree can be estimated by the dihedral angle α between the planes of the pyrone and phenyl rings (Table S5). For instance, one of the molecules that compose the asymmetric units of the methyl derivative **5** is the flattest (α = 3.3°). At the opposite, two of the molecules in the asymmetric unit of the bromine derivative **3** are twisted by 28.8° and 30.8°.

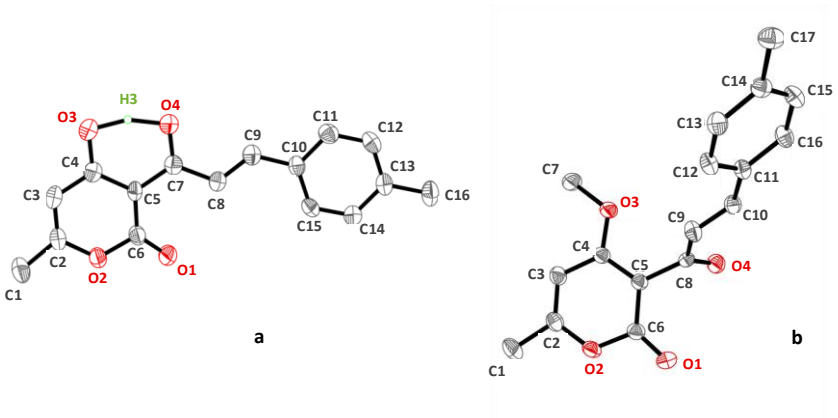

Fig. 1. Molecular structure of compounds **5** (a) and **8** (b).

In striking contrast, regarding the methoxylated CPs, the pyrone ring is twisted by 67° for **8** with respect to the cinnamoyl fragment (Fig. 1), and almost perpendicular for **9**, whose diethylamino group is slightly bulky. By comparison, this observation reveals that the intramolecular H-bond of the hydroxyl derivatives is necessary to lock the molecular structure and to make it quasi-planar.

The molecular arrangement is different for every compound. The network is mainly structured by hydrogen bonds always involving the O(1) oxygen atom of the pyrone ring and possibly the O(2), and a hydrogen atom of a neighbouring molecule. Representative examples are given in Figure 2. For most of the hydroxyl derivatives (**1**, **2**, **5**, **6** and **7**), molecules are more or less oriented along their long axis. For **1, 2** and **5**, neighboring molecules located in relatively close planes form sort of antiparallel dimers and finally assemble as layers, although each molecule of **5** also shares close contacts with its neighbours situated in higher or lower parallel planes, due to the structuring effect of the methoxy group. For **7**, molecules displayed in the same plane do not form dimers, but assemble as a continuous layer. The *tert*-butyl derivative **6** exhibits a stair-like arrangement of molecules located in parallel planes, closely intertwined with other molecules located in a very different plane (the angle between the phenyl rings of both types of molecules is about 76.3°), forming face-to-plane interactions. In this case, the *tert*-butyl groups contribute to the structuration of the network. Finally, for the bromine derivative **3**, the differently oriented molecules form sort of a herringbone structure. For all these compounds, very little overlap of the aromatic moieties was noticed when considering the molecules located in the stacking axis.

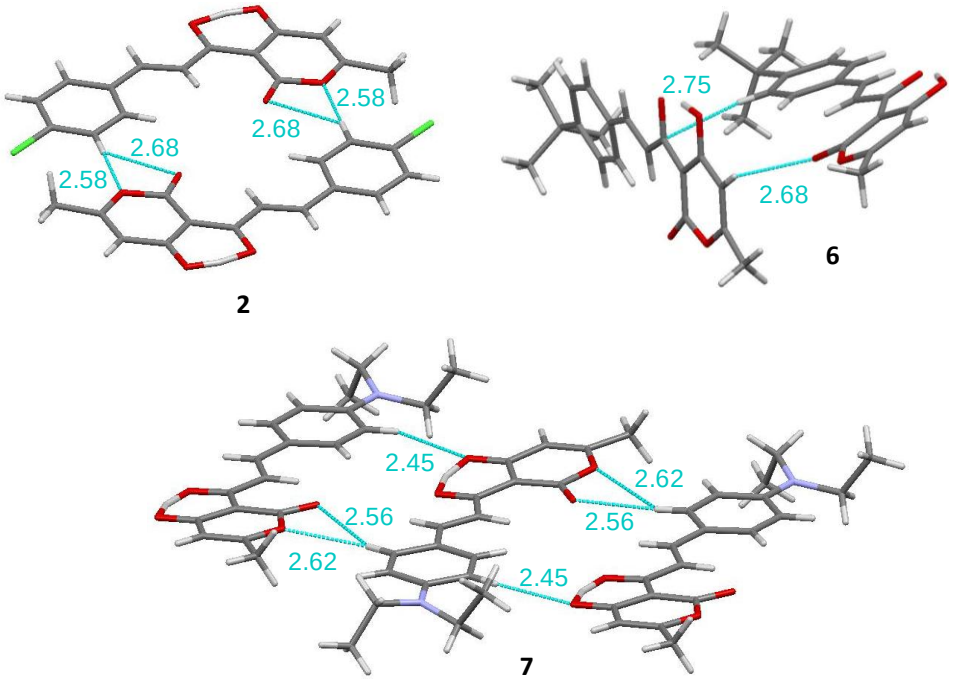

Fig. 2. Molecular arrangement in crystals of **2**, **6** and **7**. Intermolecular distances are given in Å.

Regarding the methoxylated derivatives, molecules are arranged head-to-head and form layers. For **8**, the pyrone rings assemble as columns with significant overlap between them, while in **9** they are displayed by pairs and slipped with respect to each other (Fig. 3).

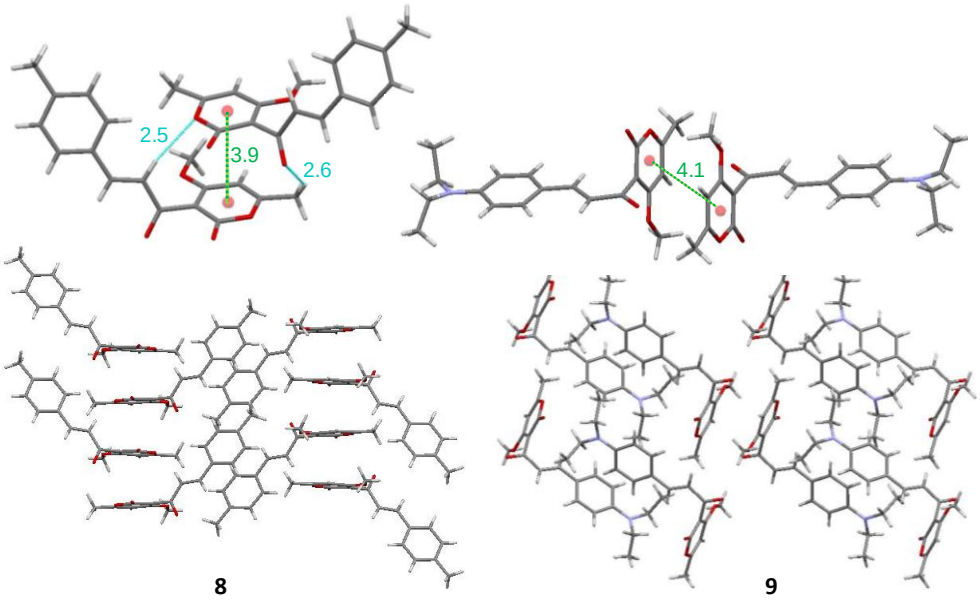

Fig. 3. Molecular arrangement in crystals of **8** (left) and **9** (right). Intermolecular distances are given in Å.

3.3. Theoretical investigation of the competing photophysical pathways

Before undertaking the experimental study, it seemed necessary to revisit the expected spectroscopic behaviour of CPs using powerful theoretical tools. TD-DFT and its spin-flip variant, SF-TD-DFT, were used to investigate the lowest singlet excited state (S_1) relaxation pathway. Specifically, the latter approach allows the correct description of conical intersections (CIs) [44], *i.e.* critical points of exact degeneracy between adiabatic electronic potential-energy surfaces of ground and excited states, where the probability of non-radiative internal conversion is very high. It is nowadays firmly established that accessible CIs play a key role in the non-radiative decay of excitation energy of molecules.

Calculations were made by first considering molecule **1** *in vacuo* as the simplest isolated representative system. Figure 4 shows that upon excitation to the $S_1(\pi,\pi^*)$ state, the system in the *trans* configuration first relaxes to a planar structure (Min-S_1-trans). Then, a favorable ESIPT process can take place producing the excited-state keto form (Min-S_1-trans-ESIPT). Min-S_1-trans-ESIPT lies 8.5 kcal/mol below Min-S_1-trans, and the ESIPT process is barrierless (at the TD-DFT level, Min-S_1-trans is not a stable intermediate and the system relaxes directly from the Franck-Condon point to Min-S_1-trans-ESIPT). Finally, a low-lying S_0/S_1 minimum energy conical intersection (S_0/S_1-trans/cis-ESIPT-MECI) can be reached by overcoming a very small excited-state potential energy barrier of 3 kcal/mol (computed at TD-DFT level both in gas phase and in dichloromethane) from Min-S_1-trans-ESIPT. The torsion dihedral angle around the ethylenic C=C double bond is ~93° at the MECI. The molecule can then efficiently return to the ground state towards the *trans* or the *cis* isomer due to the peaked topology of this conical intersection (for the interested reader, further discussion about the topology of the conical intersection seam can be found in Fig. S11). This MECI is located at a very low energy: 35 kcal/mol below the Franck-Condon region and 20 kcal/mol below Min-S_1-trans-ESIPT. It is thus most likely responsible for the very efficient non-radiative decay and photoisomerization of **1** in solution. This result is perfectly in line with the literature reports which describe this molecule as non-fluorescent at room temperature and

somewhat unstable from a photochemical point of view [26]. It is noteworthy that emission from the Min-S_1-trans-ESIPT excited-state intermediate, if any, would be expected in the 400 nm region. Inclusion of the solvent effect for dichloromethane leads to an emission energy of 3.11 eV (399 nm).

CP derivative **2**, which bears a weak electron-withdrawing substituent, was then considered. The computed S_1 excited-state potential energy barrier from the excited-state keto form (Min-S_1-trans-ESIPT) to the S_0/S_1 MECI was found to be 3.8 kcal/mol in dichloromethane, a result similar to that of CP derivative **1**.

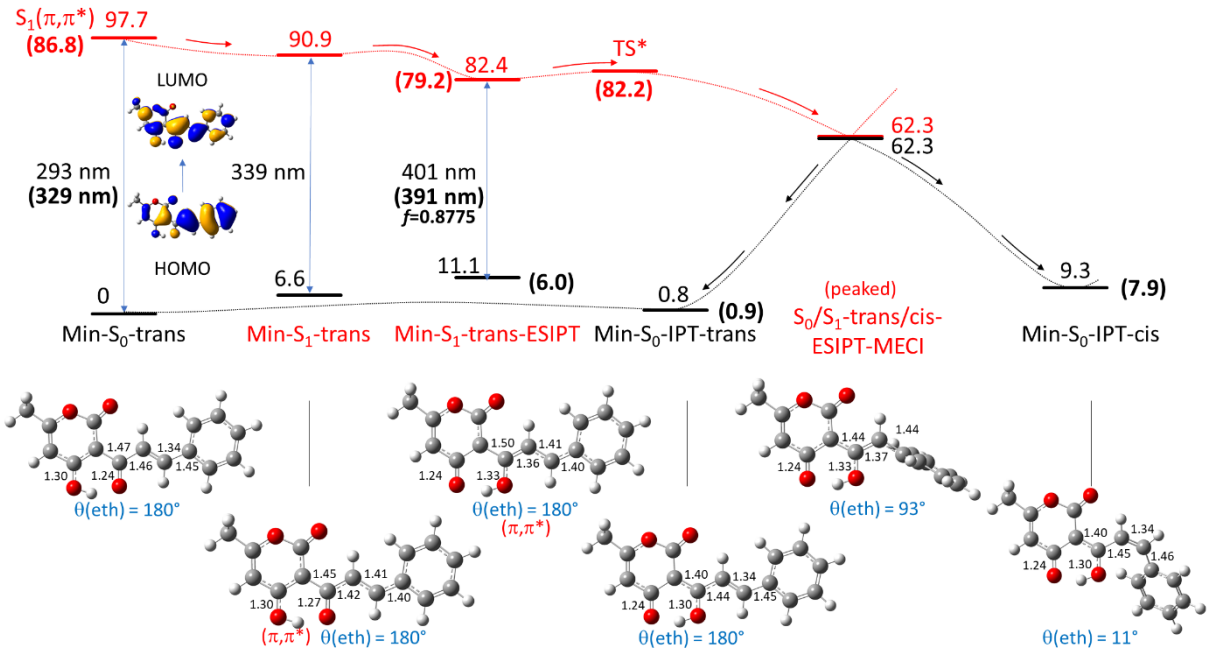

Fig. 4. Schematic potential energy profile for the isolated molecule **1** along the main S_1 excited-state relaxation pathway. Calculations are performed at the SF-TD-BH&HLYP/6-311+G** level in the gas phase. Energies are in kcal/mol with respect to the ground-state minimum (Min-S_0-trans). SF-TD-DFT values are in normal font and MN15/TD-MN15 values are in parentheses. Geometries are obtained at SF-TD-DFT level (excited-state structures are indicated in red). *f* is the oscillator strength. Relevant bond lengths are in Å. The torsion dihedral angle around the ethylenic C=C double bond (θ(eth), in blue font) involves atoms C7, C8, C9 and C10 of molecule **1** in Fig. S10 (numbering similar to that of **5** in Fig. 1a).

The occurrence of a twisted intramolecular charge transfer (TICT) process was also investigated on compound **1**. In the TICT state (Min-S_1-TICT), the torsional angle of the pyrone moiety is around 60°. The electronic structure of this TICT state results from a mixture of (π,π*) and (n,π*) contributions and involves a charge transfer from the pyrone to the cinnamoyl moiety (Fig. 5). This state is less accessible energetically than the ESIPT state (Min-S_1-trans-ESIPT), lying about 11 kcal/mol above the latter at the SF-TD-DFT level. At the TD-DFT level, Min-S_1-trans-ESIPT and Min-S_1-TICT are very close energetically (within 1 kcal/mol) in the gas phase, but upon including the dichloromethane solvent, Min-S_1-TICT raises 7 kcal/mol above Min-S_1-trans-ESIPT. If populated, it would lead to a weak emission in the 600 nm region (530 nm in dichloromethane). However, it can be expected that this emission would be quenched by the presence of a S_0/S_1 MECI lying only 5.6 kcal/mol above the TICT state. The sloped topology of this TICT MECI (in contrast to the peaked topology of

the ESIPT MECI) also means that the non-radiative decay is expected to regenerate the initial ground-state Min-S_0-trans isomer.

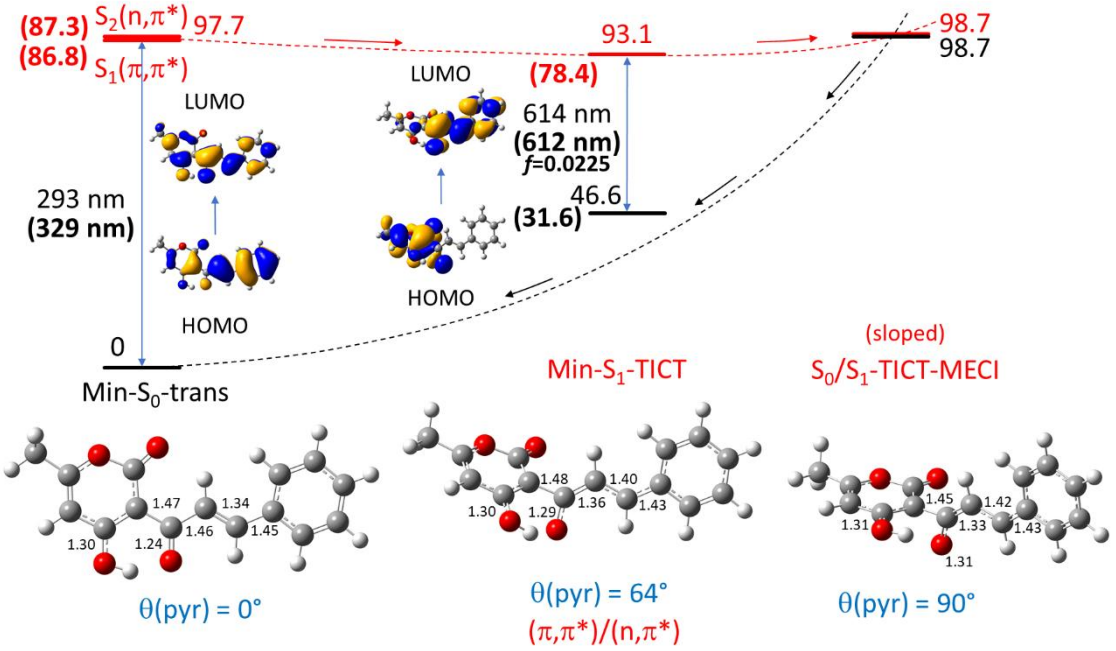

Fig. 5. Schematic potential energy profile for the TICT photophysical relaxation pathway of molecule **1**. Calculations are performed at the SF-TD-BH&HLYP/6-311+G** level in the gas phase. Energies are in kcal/mol with respect to the ground-state minimum (Min-S_0-trans). SF-TD-DFT values are in normal font and MN15/TD-MN15 values are in parentheses. Geometries are obtained at SF-TD-DFT level (excited-state structures are indicated in red). *f* is the oscillator strength. Relevant bond lengths are in Å. The torsion dihedral angle of the pyrone moiety (θ(pyr), in blue font) involves atoms C6, C5, C7 and C8 of molecule **1** in Fig. S10 (numbering similar to that of **5** in Fig. 1a). HOMO and LUMO orbitals are shown at both Min-S_0-trans and Min-S_1-TICT.

For convenience of calculation, compound **7** was investigated by considering a model molecule (**7'**) where the diethylamino group was replaced by a dimethylamino group. This strong electron-donating substituent introduces a significant ICT character in the $S_1(\pi,\pi^*)$ state compared to compound **1** (Fig. 6). The charge transfer occurs from the dimethylamino group to the pyrone moiety, in the opposite direction to that observed for the TICT state of compound **1**. Unsurprisingly, the TICT S_1 state in compound **7'** is highly destabilized to the point where no stable TICT structure could be found on the S_1 potential energy surface in this system. As a consequence, only the ESIPT relaxation channel is left in **7'**. In the isolated system, the Min-S_1-trans-ESIPT structure (keto form) lies 5.1 kcal/mol (2.5 kcal/mol at TD-DFT level) below Min-S_1-trans (enol form). While the S_0/S_1 MECI could not be located in this system due to a strong spin-contamination of the S_1 excited state in the crossing region, the excited-state barrier towards the S_0/S_1 MECI is computed at 5.6 kcal/mol (7.4 and 8.0 kcal/mol in dichloromethane and acetonitrile, respectively) at the TD-DFT level. The increase of this barrier compared to compound **1** could partly explain the increase of the luminescence quantum yield for compound **7'**. Another factor in favor of this enhanced luminescence is the increase of the oscillator strength from 1.19 in **1** to 1.50 in **7'** in dichloromethane. The vertical emission energy in **7'** is computed at 2.635 eV in dichloromethane, corresponding to an emission wavelength of 470 nm, to be compared with the experimental emission maximum of **7'** and **7** in this solvent, *i.e.* 2.15–2.16 eV (575–573 nm) based on literature [28] and our own

measurement (*vide infra*). The TD-DFT calculations overestimate the emission energy by about 0.45 eV. Note that replacing the dimethylamino group by a diethylamino group has a very weak influence on the emission energy and on the excited-state barrier, which have been calculated to be 2.615 eV / 474 nm and 7.6 kcal/mol, respectively, for **7** in dichloromethane. This validates the choice of our model system.

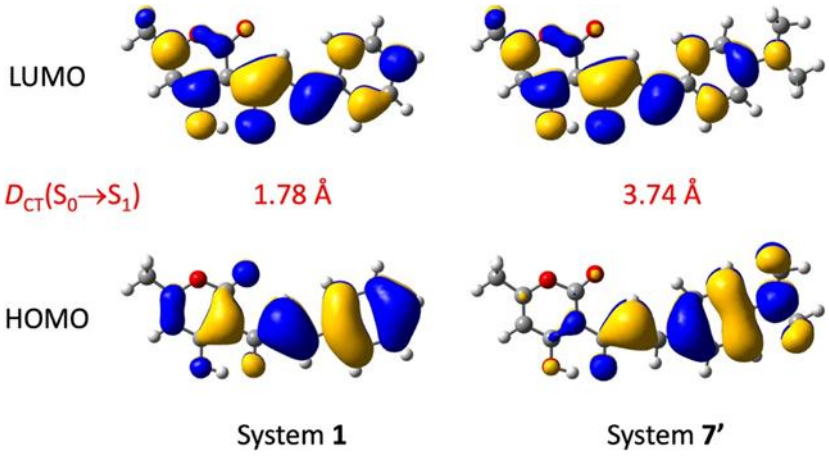

Fig. 6. Frontier orbitals of system **1** and model system **7'** (with a dimethylamino group) at the MN15/6-311+G** level in dichloromethane. The D_{CT} index is given for the $S_0 \rightarrow S_1$ transition as a measure of the charge transfer distance.

3.4. Spectroscopic study

In dichloromethane and acetonitrile solutions, the CP derivatives **1**−**6** were characterized by a strong absorption band peaking in the UV range around 360 nm and absorptivity values (ε) around 28000 $M^{-1}cm^{-1}$, with small variations depending on the weak electron donor effect of the substituent (Table 2 and Fig. S12). Compound **7** absorbed in the blue around 478-484 nm with absorptivity as high as 43000 $M^{-1}cm^{-1}$, which indicates strong ICT due to the electron-donating diethylamino group. By comparison with their respective hydroxyl analogues **5** and **7**, the methoxylated compounds **8** and **9** absorbed at much lower wavelengths (*e.g.* 312 and 402 nm, respectively in acetonitrile) and with smaller absorptivity, which may be attributed to their non-planar structure.

Our extensively-purified compounds **1**−**6** and **8** were virtually not emissive in the two solvents used. In contrast, the diethylamino derivative **7** was fluorescent, with maximum emission in the orange (576 and 590 nm in dichloromethane and acetonitrile, respectively). According to our SF-TD-DFT calculations, these values correspond to an emission from an ICT state after relaxation via an ESIPT process on S_1. The solvent effect is rather weak on the emission energy of **7**, corresponding to a decrease of the emission energy of 0.05 eV, in good agreement with the predicted red-shift of 0.03 eV. It is noteworthy that the quantum yield of **7** was 12.5-fold higher in dichloromethane than in acetonitrile. Interestingly, the methoxylated analogue **9** emitted weak green fluorescence in these solvents. The comparison between **7** and **9** highlights the advantage of the rigid structure of **7**.

The microcrystalline powders of CPs **1**−**6** appeared yellow when observed with white light. Under UV illumination, they emitted turquoise light. The photoluminescence (PL) spectra peaked between 494 and 502 nm (Fig. 7 and S13). Compound **7** was a dark pink powder, with deep red emission. Indeed, the emission spectrum peaked around 658 nm and

tailed into the IR region (Table 2). It is noteworthy that all compounds can be excited both in the UV (380 nm) and in the blue portion of the visible spectrum (470 nm). Their emission efficiency depended on the nature of the substituent. For CPs with weak electron-donor group, the best photoluminescence quantum yields (PLQY) were obtained for **4** and **5**, with value around 0.14. For the diethylamino derivative **7**, the PLQY was up to 0.32. As detailed in Table S6, the emission decays were strongly multiexponential and dependent on the emission wavelength, which suggests the involvement of molecules in various microenvironments, or the contribution of various emissive excited states. The intensity-weighted average lifetimes [45] were in the nanosecond range or below, clearly indicating the fluorescence nature of the emission, and ruling out any hypothesis of phosphorescence. We did not perform theoretical calculations in the solid state because they are very elaborated and time-consuming. However, our results acquired in the gas phase and in solution are enough to propose some relevant hypotheses about the photophysical mechanism. For compounds **1**−**6**, the fact that emission is observed in the solid state while the compounds are virtually not fluorescent in solution can be attributed to the restricted access to conical intersection (RACI), now recognized for underlying the behaviour of numerous SLE-active molecules [5, 46, 47]. In fact, due to the microenvironmental changes around the molecules, the CI is frequently higher in energy and thus less accessible in the solid state than in solutions. In the present case, molecules **1**−**6** should be blocked in the Min-S_1-trans-ESIPT state, from which they deactivate radiatively. The experimental and calculated maximum emission values are in good agreement if the packing effect is taken into account. For molecule **7**, the RACI may confine the molecules in the Min-S_1-trans-ESIPT state.

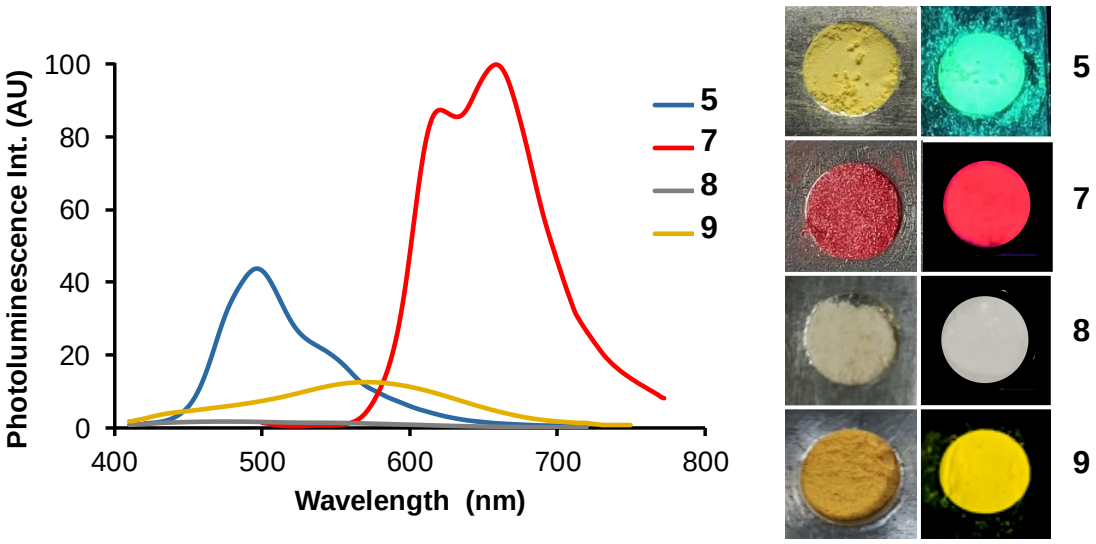

Fig. 7. Photoluminescence spectra of CPs **5** and **7**, and their methoxylated derivatives **8** and **9**, in the microcrystalline state (λ_{ex} = 380 nm). The intensity is proportional to the photoluminescence quantum yield. Insets: Samples of the corresponding as-synthesized microcrystalline powders illuminated by a hand-held UV lamp (365 nm).

The microcrystalline powders of the methoxylated derivatives **8** and **9** were respectively light beige and ocher. These compounds emitted at much shorter wavelengths, with much weaker intensity and shorter lifetimes than the corresponding hydroxyl analogues

5 and **7** (Fig. 7, Table S6 and Fig. S15). This comparison shows well that the intramolecular locking of the planar structure, and maybe ESIPT, are necessary so that CPs can emit at long wavelength and intensely in the solid state. No particular sensitivity to a mechanical stimulus was observed by grinding the as-prepared powders with a mortar and a pestle.

Compound	Solutions								Solid-state [a]			
	Acetonitrile				Dichloromethane							
	λ_{abs} (nm)	ε ($M^{-1}cm^{-1}$)	λ_{em} (nm)	Φ_F	λ_{abs} (nm)	ε ($M^{-1}cm^{-1}$)	λ_{em} (nm)	Φ_F	λ_{PL}	Φ_{PL}	$<\tau_{PL}>$' (ns)	χ_R^2
1	356	27100	nf [b]	nf	358	25100	nf	nf	500	0.08	1.05	1.077
2	358	28000	nf	nf	362	29200	nf	nf	500	0.08	1.95	1.144
3	360	29000	nf	nf	362	27200	nf	nf	502	0.04	0.58	1.248
4	356	27000	nf	nf	358	27200	nf	nf	502	0.13	1.63	1.139
5	364	28000	nf	nf	368	27000	nf	nf	498	0.14	0.95	1.176
6	366	27000	nf	nf	368	25800	nf	nf	494	0.03	0.36	1.607
7	478	43900	590	0.016	484	43700	576	0.20	658	0.32	1.56	1.218
8	312	23500	nf	nf	320	21800	nf	nf	473	<0.005	0.78	1.274
9	402	30800	488	0.007	410	31700	514	0.015	556	0.04	1.09	1.037

[a] λ_{ex} = 380 nm.
[b] nf: not fluorescent.

Table 2. Spectroscopic properties of compounds **1-9** in solution and in the solid state (as-prepared microcrystalline powders). Maximum wavelength of absorption (λ_{em}), emission (λ_{em}) and photoluminescence (λ_{PL}), molar absorption coefficient (ε), fluorescence and photoluminescence quantum yields (Φ_F and Φ_{PL}), intensity-weighted photoluminescence mean lifetimes ($<\tau_{PL}>$') and (χ_R^2) the goodness-of-fit value.

Finally, the AIE behaviour of CPs was studied using compounds **5** and **7**. As seen above, the methyl derivative **5** is not luminescent in organic solvents. The emission efficiency of the dialkylamino derivative **7** decreases markedly in a polar solvent like acetonitrile and it can be anticipated that its fluorescence will be even weaker in aqueous solvents, especially with the involvement of special deactivation mechanisms that have been shown to be ubiquitous for red emission [48]. Both compounds being strongly emissive in the solid state, and poorly soluble in water, an AIE effect can be expected. Indeed, marked spectroscopic changes were observed when increasing from 0 to 95% the fraction of water (f_w) in an acetonitrile solution of **5** and **7** at constant dye concentration (Fig. 8a,b). For **5**, almost no fluorescence was detected till f_w = 70%, and then the intensity of the emission spectra was drastically increased. The emission spectra obtained with f_w = 80-95% were reminiscent of that of the microcrystalline powder, but they were situated at lower wavelengths (468 nm *vs* 498 nm). For **7**, the spectra first underwent a red shift together with a decrease in intensity, due to the variation of solvent polarity, and then a strong emission of photoluminescence was observed. The emission spectra resembled that of the microcrystalline powder for f_w = 80% with a maximum at 658 nm, and then it underwent a small blue shift at higher water proportions. In both cases, the PL increase was associated to the formation of particles that slowly precipitate in the suspension, as illustrated for **7** in Figure S14. When observed under the fluorescence microscope, these particles were strongly emissive on a dark background. They were very thin rods for the sample of **5** prepared with 95% water, and thick crystalline platelets for **7** (Fig. 8c). This observation confirms the AIE effect, which is here particularly spectacular.

During these experiments, it was noted that the PL of the microcrystals of **7** was unchanged after prolonged observation under the strong microscope beam (λ_{ex} = 450–490 nm). In contrast, the very thin needles of **5** tended to fade, suggesting a particular photochemical sensitivity. This prompted us to observe the behaviour of native microcrystals of **5** placed directly in front of the lamp, in the absence of any filter. After 30 min irradiation,

the fluorescence of the microcrystals was completely extinguished. After dissolution of the microcrystals in $CDCl_3$, the ^1H NMR spectra showed the appearance of very small signals (Fig. S16–S19). In comparison, the irradiation of a solution of **5** (6×10^{-3} M) in $CDCl_3$ for 2h mainly led to the appearance of other signals, attributable to the *cis* form of compound **5**, *i.e.*

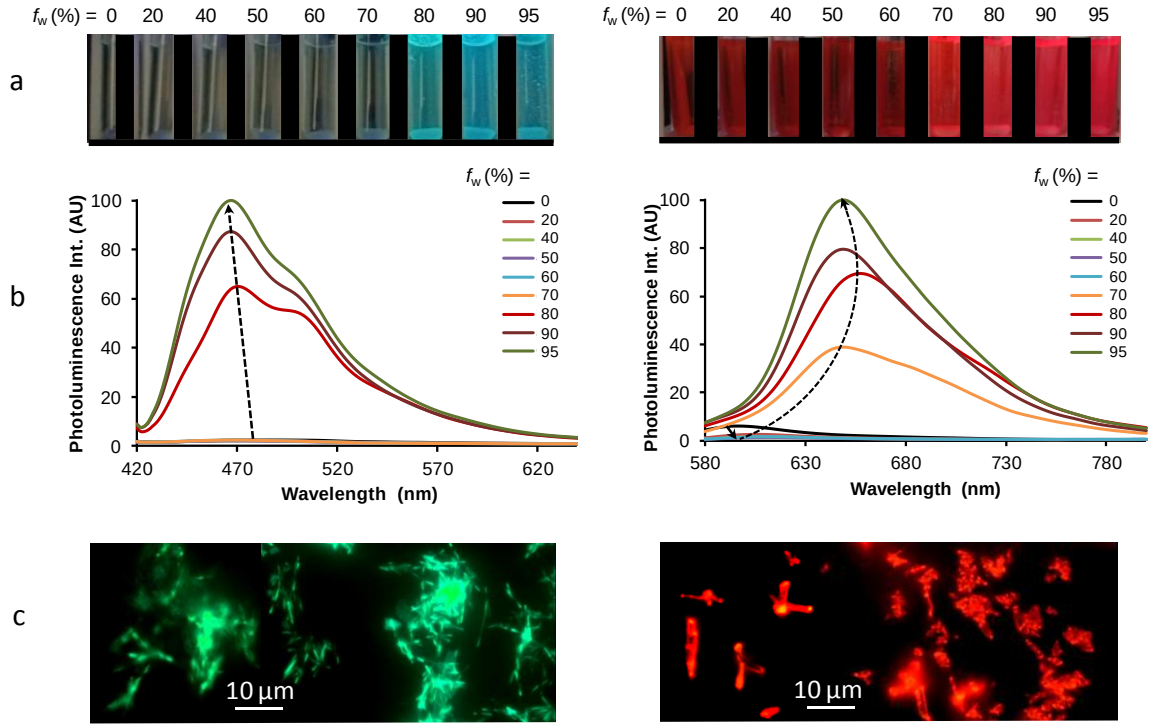

Fig. 8. a) Samples of compounds **5** (left) and **7** (right) at ~2.4×10^{-4} M in pure acetonitrile and various water/acetonitrile mixtures containing from 20 to 95% water observed upon illumination by a UV lamp at 365 nm. b) Corresponding emission spectra with excitation at 410 nm for **5** and 560 nm for **7**. The arrows indicate the evolution of the spectra with increasing the water fraction f_w. c) Fluorescence microscopy images of the samples containing 95% water.

two multiplets centered at 7.47 and 7.15 ppm (H12 and H13 protons of the benzene ring, rspectively), two doublets at 7.24 and 7.22 ppm (H9 and H10 ethylenic protons) with J = 12 Hz instead of 15.7 Hz for the *trans* form, 5.70 ppm (H5), 2.36 and 2.28 ppm (methyl groups). From the integration, the proportion of the *cis* form with respect to the *trans* form was estimated to be at around 30% in the irradiated solution. This shows that the CPs bearing a weak electron-donor substituent indeed undergo photoisomerization in solution. This process was not detected in the crystals, where it is probably quite inefficient because steric constraints prevent intramolecular motions. In contrast, another type of photoproduct is generated in the solid state, in a very small but sufficient quantity to induce a decrease of the PL efficiency. A thorough photochemical study of CPs would be instructive, but it is beyond the topic of the present study. At this stage, it can be said that compound **7** is very lightfast and the other compounds can be considered as sufficiently photostable for most of applications in the solid state.

4. Conclusion

For a long time, CP derivatives have been considered like having little interest from a spectroscopic point of view. Revisiting their photophysical behaviour made it possible to highlight the complexity of the mechanisms involved. It appeared that CPs **1**–**6** with no or weak electron donor substituents indeed undergo ESIPT in solution, but the facile access to a conical intersection subsequently induces non-radiative deactivation. Regarding the CP derivative **7**, substituted by a strong electron donor group, the presence of the latter allows the molecule to prefer another deactivation pathway in solution, through a radiative ICT state following an ESIPT process. In the solid state, where the access to CI is probably reduced, most of the CP derivatives show very attractive emission properties. In contrast to 2'-hydroxychalcones that are not emissive in the crystalline state when they bear a weak electron-donating substituent [49], CP derivatives are tunable solid-state dyes, which emit efficiently from the turquoise to the deep-red regions. This feature is far from being common for compounds prepared by a one-step synthesis, and it makes them even more attractive. In conclusion, our study rehabilitates the unjustly discarded CP derivatives, which can now find applications in the field of AIEgen-based probes and photoluminescent materials.

Acknowledgements

ANR is gratefully acknowledged for funding (SUPERFON project # ANR-17-CE07-0029-03). This work was granted access to the HPC resources of CALMIP supercomputing center under the allocation 2022-[12158].

References

[1] Gierschner J, Shi J, Milián-Medina B, Roca-Sanjuán D, Varghese S, Park SY. Luminescence in Crystalline Organic Materials: From Molecules to Molecular Solids. Adv Opt Mater 2021;9, 2002251. DOI: 10.1002/adom.202002251

[2] Zhao Q, Sun JZ. Red and near infrared emission materials with AIE characteristics. J Mater Chem C 2016;4:10588–10609. DOI: 10.1039/c6tc03359h

[3] Xu R, Dang D, Wang Z, Zhou Y, Xu Y, Zhao Y, Wang X, Yang Z, Meng L. Facilely prepared aggregation-induced emission (AIE) nanocrystals with deep-red emission for

super-resolution imaging. Chem Sci 2022;13:1270–1280. DOI: 10.1039/d1sc04254h

[4] Bera MK, Pal P, Malik S. Solid-state emissive organic chromophores: design, strategy and building blocks. J Mater Chem C 2020;8:788–802. DOI: 10.1039/c9tc04239c

[5] Suzuki S, Sasaki S, Sairi AS, Iwai R, Tang BZ, Konishi G. Principles of Aggregation-Induced Emission: Design of Deactivation Pathways for Advanced AIEgens and Applications. Angew Chem 2020;132:9940–9951. DOI: 10.1002/ange.202000940

[6] Mei J, Leung NLC, Kwok RTK, Lam JWY, Tang BZ. Aggregation-Induced Emission: Together We Shine, United We Soar! Chem Rev 2015;115:11718–11940. DOI: 10.1021/acs.chemrev.5b00263

[7] Yin Y, Hu H, Chen Z, Liu H, Fan C, Pu S. Tetraphenylethene or triphenylethylene-based luminophors: Tunable aggregation-induced emission (AIE), solid-state fluorescence and mechanofluorochromic characteristics. Dyes Pigm 2021;184:108828. DOI: 10.1016/j.dyepig.2020.108828

[8] Zhao J, Ji S, Chen Y, Guo H, Yang P. Excited state intramolecular proton transfer (ESIPT): from principal photophysics to the development of new chromophores and applications in fluorescent molecular probes and luminescent materials. Phys Chem Chem Phys 2012;14:8803–8817. DOI: 10.1039/c2cp23144a

[9] Padalkar VS, Seki S. Excited-state intramolecular proton-transfer (ESIPT)-inspired solid state emitters. Chem Soc Rev 2016;45:169–202. DOI: 10.1039/C5CS00543D

[10] Sedgwick AC, Wu L, Han HH, Bull SD, He XP, James TD, Sessler JL, Tang BZ, Tian H, Yoon J. Excited-state intramolecular proton-transfer (ESIPT) based fluorescence sensors and imaging agents. Chem Soc Rev 2018;47:8842–8880. DOI: 10.1039/c8cs00185e

[11] Kwon JE, Park SY, Advanced Organic Optoelectronic Materials: Harnessing Excited-State Intramolecular Proton Transfer (ESIPT). Adv Mater 2011;23:3615–3642. DOI: 10.1002/adma.201102046

[12] Chen L, Fu P-Y, Wang H-P, Pan M, Excited-State Intramolecular Proton Transfer (ESIPT) for Optical Sensing in Solid State. Adv Optical Mater 2021, 9, 2001952. DOI: 10.1002/adom.202001952

[13] Fery-Forgues S, Vanucci-Bacqué C, Recent trends on design, synthesis, spectroscopic behaviour and applications of benzazole-based molecules with solid-state luminescence enhancement properties. Top Curr Chem 2021;379, 32. DOI: 10.1007/s41061-021-00344-8

[14] Teshima T, Takeishi M, Arai T. Red fluorescence from tautomers of 2'-hydroxychalcones induced by intramolecular hydrogen atom transfer. New J Chem 2009;33:1393–1401. DOI: 10.1039/b823431k

[15] Yu Y, Ma L, Tan W, Cheng K, Zhou H. Amplified spontaneous emission based on an excited-state intramolecular-proton-transfer molecule with solid-state-induced emission enhancement. Opt Mater Express 2019;9:1709–1715. DOI:10.1364/OME.9.001709

[16] Tordo A, Jeanneau E, Bordy M, Bretonnière Y, Hasserodt J. Crystal-packing modes determine the solid-state ESIPT fluorescence in highly dipolar 2′-hydroxychalcones. J Mater Chem C 2021;9:12727−12731. DOI: 10.1039/D1TC03096E

[17] Cheng X, Wang K, Huang S, Zhang H, Zhang H, Wang Y. Organic Crystals with Near-Infrared Amplified Spontaneous Emissions Based on 2′-Hydroxychalcone Derivatives: Subtle Structure Modification but Great Property Change. Angew Chem Int Ed 2015;54:8369–8373. DOI:10.1002/anie.201503914

[18] Song Z, Kwok RTK, Zhao E, He Z, Hong Y, Lam JWY, Liu B, Tang BZ. A Ratiometric Fluorescent Probe Based on ESIPT and AIE Processes for Alkaline Phosphatase Activity Assay and Visualization in Living Cells. ACS Appl Mater Interfaces 2014;6:17245−17254. DOI: 10.1021/am505150d

[19] Xi MY, Sun ZY, Sun HP, Jia JM, Jiang ZY, Tao L, Ye M, Yang X, Wang YJ, Xue X, Huang JJ, Gao Y, Guo XK, Zhang SL, Yang YR, Guo QL, Hu R, You QD. Synthesis and bioevaluation of a series of a-pyrone derivatives as potent activators of Nrf2/ARE pathway (part I). Eur J Med Chem 2013;66:364–371. DOI:10.1016/j.ejmech.2013.06.007

[20] Bhat ZS, Rather MA, Lah HU, Hussain A, Maqbool M, Yousuf SK, Jabeen Z, Wani MA,

Ahmad Z. In vitro bactericidal activity of 3-cinnamoyl-4-hydroxy-6-methyl-2-pyrone (CHP) against drug-susceptible, drug-resistant and drug-tolerant isolates of Mycobacterium tuberculosis. J Global Antimicrob Resist 2020;22:57–62. DOI:10.1016/j.jgar.2019.11.018

[21] Tripathi VD. Synthesis of New Dihydropyrazoles of Designed Curcumin Analogues. Asian J Chem 2019;31:1889−1894. DOI:10.14233/ajchem.2019.22023

[22] Verma R, Bhatia R, Singh G, Kumar B, Mehan S, Monga V. Design, synthesis and neuropharmacological evaluation of new 2,4-disubstituted-1,5-benzodiazepines as CNS active agents. Bioorg Chem 2020;101:104010. DOI:10.1016/j.bioorg.2020.104010

[23] Moulkrere BR, Orena BS, Mori G, Saffon-Merceron N, Rodriguez F, Lherbet, C, Belkheiri N, Amari M, Hoffmann P, Fodili M. Evaluation of heteroatom-rich derivatives as antitubercular agents with InhA inhibition properties. Med Chem Res 2018;27:308–320. DOI:10.1007/s00044-017-2064-x

[24] Kovalska V, Chernii S, Losytskyy M, Tretyakova I, Dovbii Y, Gorski A, Chernii V, Czerwieniec R, Yarmoluk S. Design of functionalized β-ketoenole derivatives as efficient fluorescent dyes for detection of amyloid fibrils. New J Chem 2018;2:13308–13318. DOI: 10.1039/c8nj01020j

[25] Tykhanov DA, Serikova II, Yaremenko FG, Roshal AD. Structure and spectal properties of cinnamoyl pyrones and their vinylogs. Cent Eur J Chem 2010;8:347–355. DOI: 10.2478/s11532-009-0138-4

[26] Tykhanov DA, Sanin EV, Grygorovych OV, Serikova II, Yaremenko FG, Roshal AD. Photophysical and photochemical processes in cinnamoyl pyrones: influence on spectral properties and photostability. Funct Mater 2011;18:339–347.

[27] Tykhanov DA, Sanin EV, Serikova II, Yaremenko FG, Roshal AD. Cinnamoyl pyrones in proton-donating media: Electronic structure and spectral properties of protolytic forms. Spectrochim Acta Part A 2011;83:221–230. DOI:10.1016/j.saa.2011.08.022

[28] Benosmane N, Boutemeur B, Hamdi SM, Hamdi M, Silva ASM. Solvatochromic fluorescence characteristics of cinnamoyl pyrone derivatives. J Mol Struct 2017;1149:1−7. DOI: 10.1016/j.molstruc.2017.07.089

[29] Schmidt B, Hauke S. Metathesis-based De Novo Synthesis of Noviose. Eur J Org Chem 2014;9:1951−1960. DOI: 10.1002/ejoc.201301615

[30] Suzuki K, Kobayashi A, Kaneko S, Takehira K, Yoshihara T, Ishida H, Shiina Y, Oishi S, Tobita S. Reevaluation of absolute luminescence quantum yields of standard solutions using a spectrometer with an integrating sphere and a back-thinned CCD detector. Phys Chem Chem Phys 2009;11:9850–9860. DOI: 10.1039/B912178A

[31] De Mello JC, Wittmann HF, Friend RH. An improved experimental determination of external photoluminescence quantum efficiency. Adv Mater 1997;9:230–232. DOI: 10.1002/adma.19970090308

[32] Sheldrick GM. SHELXT – Integrated space-group and crystal-structure determination. Acta Cryst A 2015;71:3–8. DOI: 10.1107/S2053273314026370

[33] Sheldrick GM. Crystal structure refinement with SHELXL. Acta Cryst C 2015;71:3–8. DOI : 10.1107/S2053229614024218

[34] Macrae CF, Edgington PR, McCabe P, Pidcock E, Shields GP, Taylor R, Towler M, van de Streek J. Mercury: visualization and analysis of crystal structures. J Appl Cryst 2006;39:453–457. DOI: 10.1107/S002188980600731X

[35] Yu HS, He X, Li SL, Truhlar DG. MN15: A Kohn–Sham global-hybrid exchange–correlation density functional with broad accuracy for multi-reference and single-reference systems and noncovalent interactions. Chem Sci 2016;7:5032–5051. DOI: 10.1039/c6sc00705h

[36] Becke AD. A new mixing of Hartree–Fock and local density- functional theories. J Chem Phys 1993;98:1372–1377. DOI: 10.1063/1.464304

[37] Minezawa N, Gordon MS. Optimizing conical intersections by spin−flip density functional theory: Application to ethylene. J Phys Chem A 2009;113:12749–12753. DOI: 10.1021/jp908032x

[38] Tomasi J, Mennucci B, Cammi R. Quantum mechanical continuum solvation models. Chem Rev 2005;105:2999–3094. DOI: 10.1021/cr9904009

[39] Improta R, Scalmani G, Frisch MJ, Barone V. Toward effective and reliable fluorescence energies in solution by a new state specific polarizable continuum model time dependent density functional theory approach. J Chem Phys 2007;127:074504. DOI: 10.1063/1.2757168

[40] Le Bahers T, Adamo C, Ciofini I. A Qualitative Index of Spatial Extent in Charge-Transfer Excitations. J Chem Theory Comput 2011;7:2498–2506. DOI: 10.1021/ct200308m

[41] Frisch MJ, Trucks GW, Schlegel HB, Scuseria GE, Robb MA, Cheeseman JR, Scalmani G, Barone V, Petersson GA, Nakatsuji H, Li X, Caricato M, Marenich AV, Bloino J, Janesko BG, Gomperts R, Mennucci B, Hratchian HP, Ortiz JV, Izmaylov AF, Sonnenberg JL, Williams-Young D, Ding F, Lipparini F, Egidi F, Goings J, Peng B, Petrone A, Henderson T, Ranasinghe D, Zakrzewski VG, Gao J, Rega N, Zheng G, Liang W, Hada M, Ehara M, Toyota K, Fukuda R, Hasegawa J, Ishida M, Nakajima T, Honda Y, Kitao O, Nakai H, Vreven T, Throssell K, Montgomery JA Jr., Peralta JE, Ogliaro F, Bearpark MJ, Heyd JJ, Brothers EN, Kudin KN, Staroverov VN, Keith TA, Kobayashi R,

Normand J, Raghavachari K, Rendell AP, Burant JC, Iyengar SS, Tomasi J, Cossi M, Millam JM, Klene M, Adamo C, Cammi R, Ochterski JW, Martin RL, Morokuma K, Farkas O, Foresman JB, Fox DJ. Gaussian 16, Revision B.01. Gaussian, Inc., Wallingford CT, 2016.

[42] Barca GMJ, Bertoni C, Carrington L, Datta D, De Silva N, Deustua JE, Fedorov DG, Gour JR, Gunina AO, Guidez E, Harville T, Irle S, Ivanic J, Kowalski K, Leang SS, Li H, Li W, Lutz JJ, Magoulas I, Mato J, Mironov V, Nakata H, Pham BQ, Piecuch P, Poole D, Pruitt SR, Rendell AP, Roskop LB, Ruedenberg K, Sattasathuchana T, Schmidt MW, Shen J, Slipchenko L, Sosonkina M, Sundriyal V, Tiwari A, G. Vallejo JL, Westheimer B, Wloch M, Xu P, Zahariev F, Gordon MS. Recent developments in the general atomic and molecular electronic structure system. J Chem Phys 2020;152:154102. DOI: 10.1063/5.0005188

[43] Teimuri-Mofrad R, Rahimpour K, Gholizadeh M. Design, synthesis, characterization and fluorescence property evaluation of dehydroacetic acid-based chalcones. J Iran Chem Soc 2020;17:1103–1109. DOI:10.1007/s13738-019-01839-4

[44] Nikiforov A, Gamez JA, Thiel W, Huix-Rotllant M, Filatov M. Assessment of approximate computational methods for conical intersections and branching plane vectors in organic molecules. J Chem Phys 2014;141:124122. DOI: 10.1063/1.4896372

[45] Fišerová E, Kubala M. Mean fluorescence lifetime and its error. J Lumin 2012;132: 2059–2064. DOI: 10.1016/j.jlumin.2012.03.038

[46] Crespo-Otero R, Li Q, Blancafort L. Exploring Potential Energy Surfaces for Aggregation Induced Emission-From Solution to Crystal. Chem Asian J 2019;14:700–714. DOI: 10.1002/asia.201801649

[47] Chen Y, Lam JWY, Kwok RTK, Liu B, Tang BZ. Aggregation-induced emission: fundamental understanding and future developments. Mater Horiz 2019;6:428–433. DOI: 10.1039/c8mh01331d

[48] Maillard J, Klehs K, Rumble C, Vauthey E, Heilemann M, Fürstenberg A. Universal quenching of common fluorescent probes by water and alcohols. Chem Sci 2021;12:1352–1362. DOI:10.1039/D0SC05431C

[49] Serdiuk IE, Wera M, Roshal AD. Structural and Spectral Features of 4′-Substituted 2′-Hydroxychalcones in Solutions and Crystals: Spectroscopic and Theoretical Investigations. J Phys Chem A 2018;122:2030−2038. DOI: 10.1021/acs.jpca.7b10361